



In-situ photocalorimetry-fluorescence spectroscopy studies of RhB photocatalysis over Z-scheme g-C₃N₄@Ag@Ag₃PO₄ nanocomposites: A pseudo-zero-order rather than a first-order process

Xingxing Li ^a, Ting Wan ^a, Jianyuan Qiu ^a, Hui Wei ^c, Fanghong Qin ^a, Yihui Wang ^a, Yanjuan Liao ^c, Zaiyin Huang ^{a,b,*}, Xuecai Tan ^{a,b}

^a College of Chemistry and Chemical Engineering, Guangxi University for Nationalities, Nanning, 530006, China

^b Key Laboratory of Forest Chemistry and Engineering, Guangxi University for Nationalities, Nanning, 530006, China

^c College of Marine Science and Biotechnology, Guangxi University for Nationalities, Nanning, 530006, China



ARTICLE INFO

Article history:

Received 18 February 2017

Received in revised form 26 April 2017

Accepted 29 May 2017

Available online 1 June 2017

Keywords:

g-C₃N₄@Ag@Ag₃PO₄

Z-scheme photocatalysis

Photocalorimetry

Thermodynamics

Photocatalytic mechanism

ABSTRACT

Much effort has been expended recently to apply photocatalysis to address the environmental crises and energy shortage crises. However, it is controversial to demonstrate that photocatalytic kinetics follows a pseudo-first-order process by common spectroscopy, because it only reflects the variation of chromophoric groups vs. time in the initiating photocatalysis, ignoring the subsequent intermediates oxidation. In this study, we used a photocalorimetry-fluorescence spectrum, coupling of a photocalorimeter and a laser-induced fluorescence spectroscopy, to demonstrate it is a pseudo-zero-order rather than a first-order process. It shows the feasibility to investigate not only photocatalytic kinetics but also reaction pathway and rate-determining step. During RhB photocatalysis over g-C₃N₄@Ag@Ag₃PO₄, three main heat changes occurred: (ab) the photoresponse of Rhodamine B molecules and the photocatalyst, consequently generating both hydroxyl and superoxide radicals, (bc) the balance between endothermic photoresponse and exothermic RhB photodegradation by O₂^{•-}/OH and finally (cd) a stable exothermic period of RhB photodegradation. Specifically, the photocatalysis underwent an initial endothermic reaction and a subsequent exothermic stage, and eventually maintained a stable exothermic rate of $-(0.2345 \pm 0.0971) \text{ mJ s}^{-1}$ with a pseudo-zero-order process. With Ag NPs working as a bridge, the g-C₃N₄@Ag@Ag₃PO₄ system followed a Z-scheme mechanism, simultaneously generating both hydroxyl and superoxide radicals. Therefore, N-demethylation and chromophore cleavage rapidly occurred within 10 min. Then the ring cleavage and the oxidation of intermediates which were the rate-determining step eventually dominated, corresponding to the cd stage with a pseudo-zero-order process, and resulting in a pseudo-zero-order rather than a first-order process in RhB photocatalysis over g-C₃N₄@Ag@Ag₃PO₄.

© 2017 Elsevier B.V. All rights reserved.

1. Introduction

Current progress in heterogeneous photocatalysis is highlighted in solar energy conversion and storage, including water splitting, organic synthesis, environmental remediation, CO₂ photoreduction and antibacterial applications [1,2]. Up to now, the development of photocatalysts with high efficiency, long-term stability and eco-friendliness for practical applications is always receiving considerable attention [2–5]. On the other hand, understanding of the photocatalytic mechanism has struggled to keep up because most

of these photocatalysis involve multiple reactions that are difficult to characterize with current analytical techniques, which is one of the indispensable factors for making substantial breakthroughs for practical application of photocatalysts [6]. Hence, an alternative method or instrument for *in situ* characterization of the photocatalytic mechanism is really needed [7].

Significant progress has been made in studying *in-situ* catalytic processes, including the use of *in-situ* spectroscopy [8,9], *in-situ* X-Ray absorption techniques [10] and *in-situ* small-angle X-ray scattering [11]. By taking advantage of the measurement of heat changes and thermokinetics with simultaneous sample irradiation [12,13], photocalorimetry (PC) provides an alternative approach to thermodynamically study *in-situ* photoreactions and has been used extensively for the determination of quantum

* Corresponding author at: College of Chemistry and Chemical Engineering, Guangxi University for Nationalities, Nanning, 530006, China.

E-mail address: huangzaiyin@163.com (Z. Huang).

efficiency in complicated photoreactions [14–23], photostability evaluation of light-sensitive substances [22–26], and photopolymerization kinetics [27–29]. LED-photocalorimetry (LED-PC) was designed in our laboratory by introducing LED light into an RD496L microcalorimeter using optical fibers, which was used to study *in situ* photocatalysis thermodynamically by tracing thermodynamics and kinetics in real-time [7]. The work principle of LED-PC is based on a heat-conduction principle, in which sample cell and reference cell are surrounded by a heat-sink [12,13]. Any heat variation is exchanged quantitatively with the heat-sink, and the temperature difference between the sample and the reference is converted to a power signal and recorded [7]. However, heat changes measured by a photocalorimeter in the beginning of photocatalysis were macroscopical and the sum of multiple reactions, in which mainly occurred photoresponse of photocatalyst and then balance between endothermic photoresponse and pollutant photodegradation [7]. Besides, thermokinetics of photocatalysis derived from heat releases were lagged behind its heat changes. Herein, to overcome the relaxation effects of thermokinetics and obtain sophisticated information of photoreaction, we report the coupling of a photocalorimeter and an *in-situ* fluorescence spectroscopy to incorporate analysis of photoreaction.

Recently, fluorescence spectroscopy has been widely used as a rapid and effective method to assess wastewater quality in tracking sources of pollution and treatment processes [30]. In general, compared to natural waters, wastewater presents higher fluorescence intensity for the components containing cellular material and their exudates or fluorescence compounds. Compared with expensive or time-consuming techniques which offered only snapshots of moments in time [31,32], such as biochemical oxygen demand (BOD), chemical oxygen demand (COD) and total organic carbon (TOC), fluorescence spectroscopy has multiple advantages: it is fast, inexpensive, reagentless, requires little sample preparation, is highly sensitive and non-invasive [33–35]. Meanwhile, fluorescence monitoring could provide rapid feedback, allowing dynamic, high spatial and temporal resolution studies [36]. Thus, it makes fluorescence spectroscopy suitable for online monitoring in wastewater treatments. Therefore, we coupled of the photocalorimeter and an *in-situ* fluorescence spectroscopy to incorporate analysis of photocatalysis thermodynamically by tracing thermodynamics and kinetics in real-time.

In this work, first, Z-scheme $\text{g-C}_3\text{N}_4@\text{Ag}@\text{Ag}_3\text{PO}_4$ nanojunctions with Ag NPs embedded in the interface of $\text{g-C}_3\text{N}_4$ and Ag_3PO_4 are synthesized via the etching of $\text{g-C}_3\text{N}_4@\text{Ag}$ by aqueous solutions of Fe^{3+} containing a certain amount of H_2PO_4^- , in which Ag NPs, with a large work function, work as a bridge for fabricating the recombination of h^+ in the VB of $\text{g-C}_3\text{N}_4$ and e^- in the CB of Ag_3PO_4 . Secondly, to better understand the photocatalytic pathway, active species and degradation intermediates were determined by electron paramagnetic resonance (EPR) and ultrahigh performance liquid chromatography-mass spectrometry (UPLC-MS), respectively, and we use the photocalorimeter-fluorescence spectrum to investigate photocatalytic kinetics and degradation pathway of RhB photocatalysis by tracing thermodynamics and kinetics in real-time.

2. Construction of a novel photocalorimeter-fluorescence spectrum (PC-PL)

Based on the previous LED-PC [7], we designed a novel photocalorimetry-fluorescence spectrum, which includes a photocalorimeter and a laser-induced fluorescence spectroscopy with 405-nm laser. Specifically, monochromatic light (405-nm laser with 1-nm half peak width) was introduced into both sample cell and reference cell of the microcalorimeter by fiber optics in Fig. 1a,

meanwhile, another parallel fiber optic installed in the sample cell was applied to transmit the photoinduced fluorescence originating from the photocatalysis to a spectrometer (USB4000-FL, Ocean Optics, Florida, USA). Specifically, the incident 405 nm-laser passes a lens and converted to parallel light, going through a dichroic and band-pass filter, finally focusing on the sample cell by a convex lens; While the photoinduced fluorescence is transmitted to the spectrometer through the scattering path and two consecutive reflexes by a mirror and the dichroic, respectively, finally collecting to the spectrometer, as shown in Fig. 1b. The reason for choosing this laser as a source is that it has the features of good brightness, monochromaticity, anti-jamming, coherence, penetrability, and it is highly efficient with minimal energy burned off as heat with a cold light wavelength. A 405 nm-laser with a tunable intensity was used as an excitation light source of both photocatalysis and the fluorescence spectrum.

The incident light intensity in Fig. S1a of two cells were adjusted roughly outside of the photocalorimeter and determined 20 times using a solar power meter (TES-1333, TES Electrical Electronic Corp., Taiwan, China), which was $19.15 \pm 0.14 \text{ W m}^{-2}$ for the reference cell and $19.53 \pm 0.20 \text{ W m}^{-2}$ for the sample cell. The baseline was adjusted to zero by fine tuning of light intensity and is shown in Fig. S1b. To offset the baseline shift because of the trace heat deviation produced by the differential intensity of two cells, a blank was used to record the heat changes generated by irradiation of the reference and the sample cell charged with 1.0 mL deionized water under identical conditions. Prior to using the integrated system, the laser-photocalorimeter was calibrated by determination of standard molar reaction enthalpy of the photolysis of potassium ferrioxalate at 298.15 K, which is $-(59.9425 \pm 2.7298) \text{ kJ mol}^{-1}$ and is very close to the value in the literature [7,15], which indicates that the instrument is reasonable and reliable (please see Fig. S2 and the Supporting information for more details).

3. Results and discussion

3.1. Synthesis and characterization of $\text{g-C}_3\text{N}_4@\text{Ag}@\text{Ag}_3\text{PO}_4$

3D tremella-like $\text{g-C}_3\text{N}_4$ (denoted as CN) was prepared via a facile thermal polymerization method. The XRD image of the as-prepared $\text{g-C}_3\text{N}_4$ in Fig. S3 show two peaks at 13.2° and 27.5° , corresponding to the (100) and (002) planes the graphite-like carbon nitride [37]. The SEM images of the $\text{g-C}_3\text{N}_4$ in Fig. 2a show essentially the tremella-like morphology composing of irregularly assembled nanosheets with a thickness of less than 10 nm. The TEM analysis in Fig. 2b find that 3D tremella-like $\text{g-C}_3\text{N}_4$ is consisted of nanosheets and crosswise nanowires with a diameter of about 30 nm. The zeta potential of the $\text{g-C}_3\text{N}_4$ suspension in Fig. S4 ranges from -15.56 to -25.79 mV when the pH changes from 5 to 7, indicating that its surface possesses a negative charge which could interact well with the Ag^+ , facilitating the uniform decomposition of Ag NPs on the surface of $\text{g-C}_3\text{N}_4$. Consequently, the SEM image of $\text{g-C}_3\text{N}_4@\text{Ag}$ with a 12% Ag NPs content (denoted as CNA12%) in Fig. S5a show that the Ag NPs with a diameter of about 10 nm are uniformly deposited on the surface of $\text{g-C}_3\text{N}_4$, whose actual Ag NPs content eventually turned out to be 0.57%. Its XRD images in Fig. S3 show two peaks at 13.2 and 27.5° , corresponding to the (100) and (002) planes of the graphite-like carbon nitride [37], and three peaks at 38.2 , 44.2 , and 64.5° , corresponding to the (111), (200), and (220) planes of Ag (JCPDS No. 04-0783) [27], respectively.

The Z-scheme $\text{g-C}_3\text{N}_4@\text{Ag}@\text{Ag}_3\text{PO}_4$ (denoted as CNAAP) with Ag NPs embedded in the interface of $\text{g-C}_3\text{N}_4$ and Ag_3PO_4 were synthesized via the etching of $\text{g-C}_3\text{N}_4@\text{Ag}$ by aqueous solutions of Fe^{3+} containing a certain amount of H_2PO_4^- . In view of the generation of possible precipitation in the mixture solution, the optimum con-

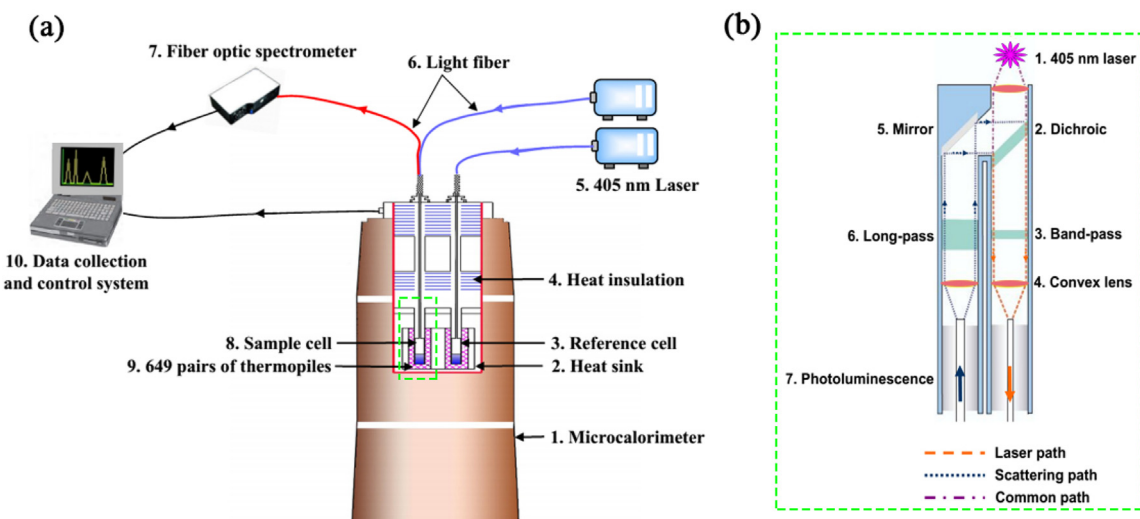


Fig. 1. Schematic illustration of a photocalorimeter-fluorescence spectroscopy (a) and optical probe in sample cell (a).

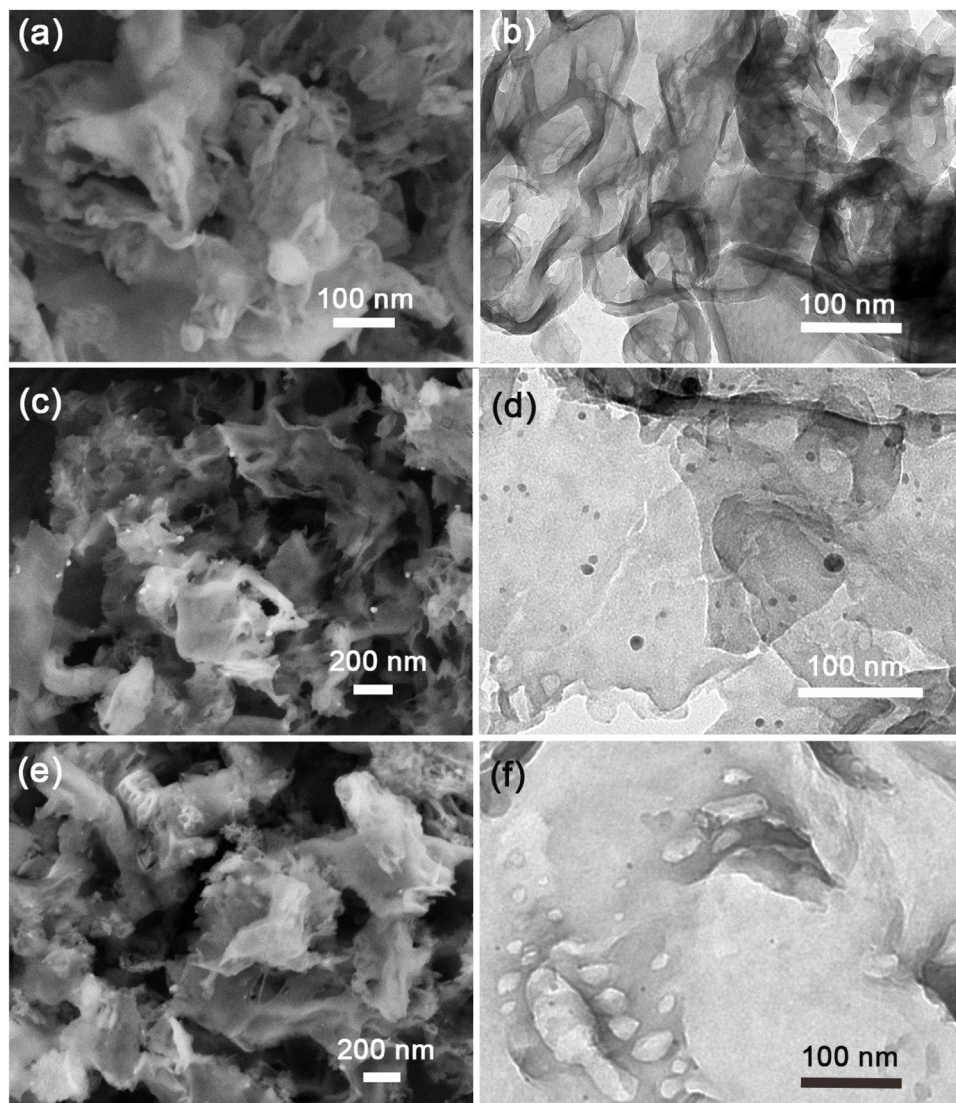


Fig. 2. SEM and TEM images of 3D tremella-like CN (a) and (b), CNAP1 (c) and (d), and CNAAP 30% (e) and (d), respectively.

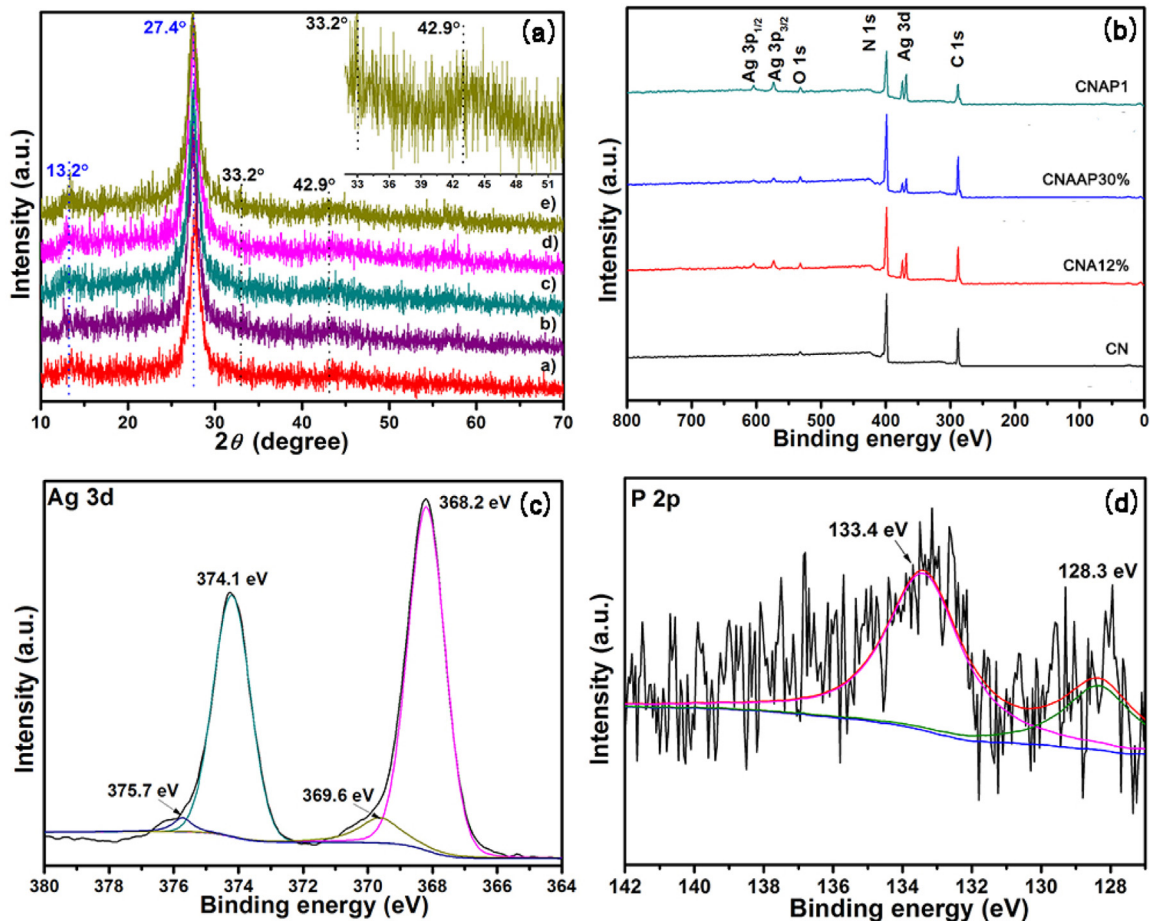
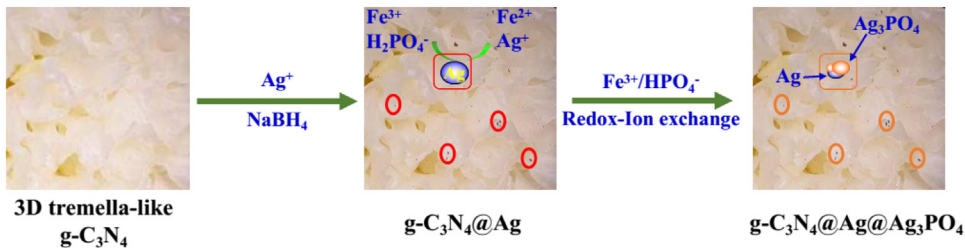


Fig. 3. XRD pattern (a) of CNAAP5% a), CNAAP10% b), CNAAP20% c), CNAAP30% d), and CNAAP50% e) and the inset: diffraction peak of Ag_3PO_4 nanoparticles at 33.2° and 42.9° . Survey XPS spectrum (a) of CN, CNA12%, CNAAP30%, and CNAP1. XPS spectra of CNAAP30%: Ag 3d (c), P 2p (d), respectively.



Scheme 1. Schematic route for synthesis of Z-scheme $\text{g-C}_3\text{N}_4@\text{Ag}@\text{Ag}_3\text{PO}_4$ nanocomposites.

centration and ratio of Fe^{3+} and H_2PO_4^- were confirmed (please see Fig. S6). First, CNA12% was synthesized using NaBH_4 as a reductant, whose SEM images in Fig. S5a show the uniform decomposition of Ag NPs on the surface of $\text{g-C}_3\text{N}_4$. Next, parts of the Ag NPs were oxidized by Fe^{3+} in the presence of an aqueous solution containing a certain ratio of Fe^{3+} and H_2PO_4^- . The standard electrode potential of the $\text{Fe}^{3+}/\text{Fe}^{2+}$ couple ($E^\theta = +0.771 \text{ V}$ vs. SHE) was more positive than that of $\text{Ag}/\text{Ag}_3\text{PO}_4$ ($E^\theta = +0.45 \text{ V}$ vs. SHE) [38,39]. Thus, electrons transfer from the surface of Ag NPs to Fe^{3+} and the generated Ag^+ is combined with H_2PO_4^- to form Ag_3PO_4 . The XRD images in Fig. 3a and XPS spectra in Fig. 3b of the $\text{g-C}_3\text{N}_4@\text{Ag}@\text{Ag}_3\text{PO}_4$ samples also show no peaks of ferric compounds, indicating that no ferric precipitation occurred under these conditions. In this work, 5% of the Ag NPs were theoretically oxidized to Ag_3PO_4 , therefore, the product ($\text{g-C}_3\text{N}_4@\text{Ag}@\text{Ag}_3\text{PO}_4$ with 5% of Ag NPs content) was denoted as CNAAP5%. Similarly, CNAAP10%, CNAAP20%, CNAAP30%

and CNAAP50% with different Ag NPs content were also synthesized using the same processes. For comparison to the photocatalysts, $\text{g-C}_3\text{N}_4@\text{Ag}_3\text{PO}_4$ nanocomposites (denoted as CNAP) with different Ag_3PO_4 content were synthesized (see Fig. S7 and S8). The XRD and SEM images of the CNAP samples are presented in Fig. S7 (Scheme 1).

The transmission electron microscopy (TEM) analysis in Fig. 2f shows that the $\text{Ag}@\text{Ag}_3\text{PO}_4$ NPs in the $\text{g-C}_3\text{N}_4@\text{Ag}@\text{Ag}_3\text{PO}_4$ 30% samples are anchored evenly over the $\text{g-C}_3\text{N}_4$ substrate and have an average size of 5.6 nm. As a result of the photocorrosion of the deposited Ag_3PO_4 NPs under irradiation of high-energy electrons, it is difficult to obtain high-resolution TEM. The XRD images of all the CNAAP samples in Fig. 3a show two peaks at 13.2 and 27.5° , corresponding to the (100) and (002) planes of the graphite-like carbon nitride [37]. The two weak peaks at 33.2 and 42.9° in the

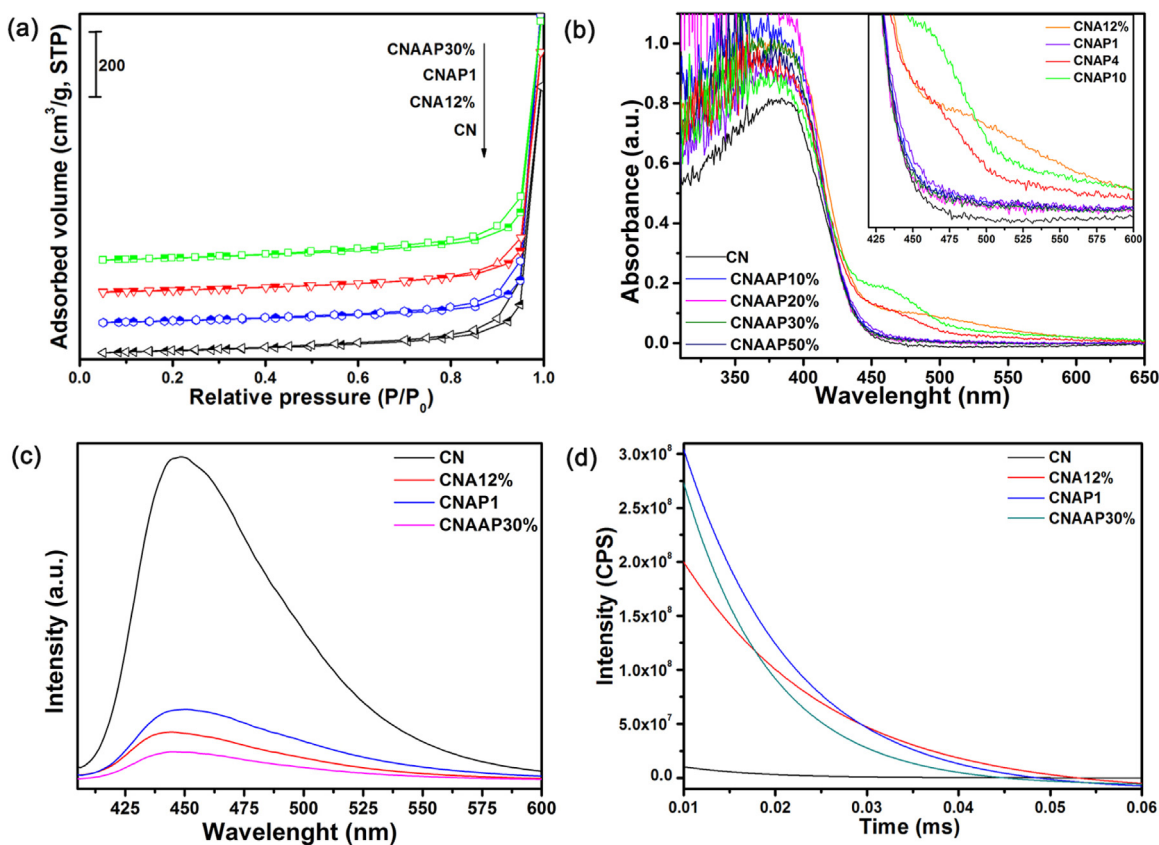


Fig. 4. N_2 adsorption-desorption isotherms (a), UV-vis diffuse reflection spectra (DRS) of as-prepared samples and the inset: the enlarged DRS of CNA12%, CNAP1, CNAP4, and CNAP10 (b), PL spectra excited at 395 nm (c), and decay curves monitored at 444 nm of CN, CNA12%, CNAP1, and CNAAP30% (d).

inset of Fig. 3a correspond to the (210) and (220) planes of Ag_3PO_4 (JCPDS No. 06-0505), respectively.

To determine the existence of Ag NPs and Ag_3PO_4 , X-ray photoelectron spectroscopy (XPS) was used to study the elemental composition and chemical status of the as-prepared $\text{g-C}_3\text{N}_4@\text{Ag}@\text{Ag}_3\text{PO}_4$. As shown in Fig. 3b, there are no peaks for other elements except for Ag, O, C and N in the XPS survey spectra of CN, CNA12%, CNAAP30% and CNAP1, indicating that there are no other impurities in these samples. Fig. 3c shows that the Ag 3d spectrum consists of two individual peaks at approximately 368.2 and 374.1 eV, which could be ascribed to binding energies of Ag 3d_{5/2} and Ag 3d_{3/2}, respectively. Both Ag 3d_{5/2} and Ag 3d_{3/2} peaks can each be divided into two peaks at 368.2 and 369.6 eV as well as 374.1 and 375.1 eV, respectively, where the peaks at 368.2 and 374.1 eV are for the Ag⁺ of Ag_3PO_4 , and those at 369.2 and 375.1 eV are attributed to metallic Ag⁰ [37,40,41]. The broad peak in the range of 131–136 eV of the P 2p [41] and 128.3 eV of the 2p_{1/2} spectrum [42] in Fig. 3d corresponds to the phosphorous from Ag_3PO_4 . As for the real composition of CNAAP30%, its XPS result shows the atom content of Ag and P in CNAAP30% nanocomposites is about 3.57% and 0.37%, respectively. And the ratio of Ag⁰ to Ag⁺ was calculated to be 1.79, therefore, the real Ag⁺ content in the Ag element is about 35.8%. XPS spectra of C 1s, N 1s, and O 1s of CNAAP30% presents in Fig. S9.

The isotherms and hysteresis loops of CN, CNA12%, CNAAP30%, and CNAP1 ($\text{g-C}_3\text{N}_4@\text{Ag}_3\text{PO}_4$ with 1.0 mM of Ag_3PO_4 content) in Fig. 4a have a similar type and belong to a typical type IV isotherm and type H3 loop (based on the IUPAC classification), indicating the presence of mesopores [43]. The BET specific surface areas of CN, CNA12%, CNAAP30%, and CNAP1 are 81.6, 81.9, 88.5 and 78.3 $\text{m}^2 \text{g}^{-1}$, respectively. Fig. 4b presents the UV-vis diffuse reflectance spectra of CN, CNA12%, CNAAP30%, and CNAP1.

The pure $\text{g-C}_3\text{N}_4$ and Ag_3PO_4 have a maximum absorption in the visible region at about 450 and 530 nm, respectively. As for the $\text{g-C}_3\text{N}_4@\text{Ag}_3\text{PO}_4$, the absorption intensity in the region from 430 to 530 nm gradually weakens with decreasing the Ag_3PO_4 content. CNAP1, with the highest photocatalytic efficiency in all the CNAP, has the low absorption in this region for the trace amount of Ag_3PO_4 content, indicating that the photocatalytic activity is directly related to the uniform deposition and sizes of Ag_3PO_4 NPs rather than their contents (see Fig. S7 and S8). Similarly, CNAAP30% with a maximum absorption edge at about 450 nm have the greatest photocatalytic activity, as shown in Fig. 5. According to the plots of $(Ah\nu)^2$ against the energy of the absorbed photon, the band gaps (E_g) of $\text{g-C}_3\text{N}_4$ and Ag_3PO_4 were estimated to 2.81 and 2.38 eV (as shown in Fig. S10), respectively [37,41,44]. Meanwhile, the conduction band potential E_{CB} and the valence band E_{VB} of $\text{g-C}_3\text{N}_4$ were calculated to be -1.19 and 1.63 eV vs. NHE, respectively, and those of Ag_3PO_4 were +0.27 and 2.65 eV vs. NHE, respectively (please see the supporting information).

It is well known that a lower PL intensity indicates a lower recombination of charge carriers, leading to higher photocatalytic activity [37]. Compared with the pure CN in Fig. 4c, the obviously decreased PL intensity of CNA12%, CNAP1 and CNAAP30% can be attributed to the decomposition of Ag NPs or Ag_3PO_4 . Whereas the PL intensity of CNAAP30% with Ag NPs embedded in the interface of $\text{g-C}_3\text{N}_4$ and Ag_3PO_4 has the lowest peak, indicating that it possesses a lower recombination of charge carriers, leading to the greater photocatalytic activity, which is in agreement with the photocatalytic activity shown in Fig. 5. The relaxation courses of carrier dynamics of photocatalysts were widely recorded by time-resolved spectra to investigate photogenerated charge carrier behaviors [45]. Compared with $\text{g-C}_3\text{N}_4$, the transient signals at 444 nm (Fig. 4d) of CNA12%, CNAP1, and CNAAP30% exhibit greatly

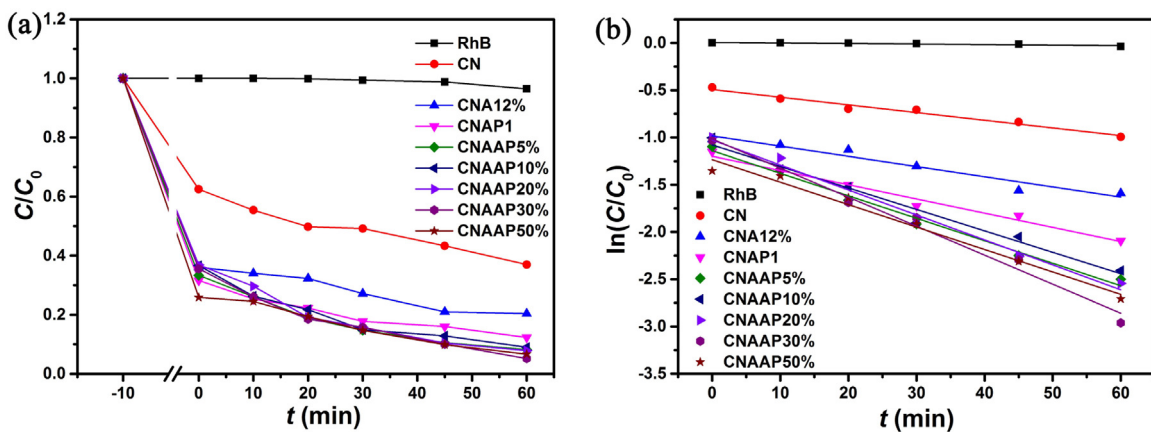


Fig. 5. Photocatalytic degradation of RhB over CN, CNA12%, CNAP1, CNAAP5%, CNAAP10%, CNAAP20%, CNAAP30%, and CNAAP50% under visible-light irradiation (a) and plots of $\ln(C/C_0)$ vs. time (b).

Table 1

Heat changes of different stages and the stable exothermic rate of cd (R_{cd}).

Entry	Heat changes (J) ^a			R_{cd} (mJ s ⁻¹) ^b	$k \times 10^{-3}$ (min ⁻¹) ^c
	ab	bc	cd		
RhB	–	–	–	–0.2506	–0.0054
CN	0.0088	–0.0439	–0.3343	–0.3694	8.1400
CNAP1	0.0408	–0.0066	–0.7903	–0.7561	15.0590
CNAAP30%	0.0502	–0.00691	–1.0977	–1.0544	30.1180

^a Integrated area of the heat changes curve of different stages.

^b The stable exothermic average rate of cd stage measured by the photocalorimeter.

^c The rate constant of degradation of the chromophoric groups measured by a UV-vis spectra. The whole illumination time of ad stage in each entry is 3600 s.

retarded decay kinetics. The relatively long lived charge separation state can increase the probability of charge carriers participating in photocatalytic redox reactions [45].

3.2. Photocatalytic activity

The surface adsorption efficiency of RhB over CNAAP30% is almost 1.84 times higher than that of the g-C₃N₄ in Fig. 5a. The zeta potential of CNAAP30% in Fig. S4 is more negative than that of the g-C₃N₄ in the range of pH from 5 to 7. Therefore, when mixed with cationic RhB molecules, CNAAP30% exhibits higher adsorption efficiency owing to the more stronger electrostatic interaction, eventually facilitating photocatalytic activity. According to the first-order reaction, the slope of plots of $\ln(C/C_0)$ vs. time detected by UV-vis spectra was always used to determine the rate constant by the equation $\ln(C_0/C) = kt$ [37–41,46–49]. Actually, the rate constant were only reflected the variation of chromophoric groups vs. time in the beginning of photocatalysis rather than that including subsequently the ring cleavage and the oxidation of intermediates. For comparison to the photocatalysts, g-C₃N₄@Ag₃PO₄ (denoted as CNAP) with different Ag₃PO₄ contents were synthesized. As shown in Fig. 5a, CNAAP30% exhibited higher photocatalytic efficiency than that of CNA12%, CNAP1, and other CNAAP, the degradation rate within 60 min was up to 94.8% and its rate constant of degradation of the chromophoric groups in Table 1 is almost 3.7 times higher than that of the CN, 2.85 times higher than that of the CNA12% and 2.0 times higher than that of CNAP1.

3.3. Possible photocatalytic mechanism

It is shown in Fig. S11a that the CNAAP(5%–50%) have the peak locations and characteristic 1:2:2:1 relative peak magnitudes, which are attributed to trapped hydroxyl radicals in the form of DMPO-OH [44,46]. The CNAAP30% exhibits much higher

intensity than other g-C₃N₄@Ag@Ag₃PO₄. Meanwhile, as shown in Fig. S11b, the CNAAP(5%–50%) also have characteristic peaks of DMPO-•O₂[−]/OOH adducts signals with an intensity ratio of 1:1:1:1 [44,46]. Compared with CN, CNA12%, and CNAP1 in Fig. 6a, only the CNAAP30% have the characteristic peaks of DMPO-OH adduct signals, attributed to the holes on the VB of Ag₃PO₄ oxidizing OH[−] to •OH, since its VB potential is more positive than E_0 (OH[−]/•OH) (+2.31 eV vs. NHE, as shown in Fig. 7) [7]. In Fig. 6b, CN, CNA12%, and CNAAP30% all have characteristic peaks of DMPO-•O₂[−]/OOH adduct signals, which may result from reducing O₂ to •O₂[−] since their VB potential of g-C₃N₄ is more negative than E_0 (O₂/•O₂[−]) (−0.046 eV vs. NHE, as shown in Fig. 7b). As for CNAP1 hybrids, only weak signals of DMPO-•O₂[−]/OOH adducts were observed in Fig. 6b (marked with green dashed boxed), indicating that charge transfer in the interface of the CNAP1 is driven by the ohmic contact in Fig. 7a [47,48]. Owing to the less content of Ag₃PO₄ deposited on g-C₃N₄ matrix, the photo-generated electrons of g-C₃N₄ could not only directly injected into the CB of Ag₃PO₄ but also react with oxygen molecules to generate weak •O₂[−] radicals. Specifically, the electrons that are photogenerated from g-C₃N₄ with a higher CB edge migrate to Ag₃PO₄ with a lower CB edge. Moreover, the photogenerated holes are transported from the high VB of Ag₃PO₄ to the low VB of g-C₃N₄ [37,46]. The peak locations marked by blank circles in Fig. 6a and b may be caused by DMPO self-decomposition. Meanwhile, the blank that contains only RhB solution shows the absence of hydroxyl radicals and superoxide radicals.

Based on the above results and discussion, the photoresponse mechanism scheme for RhB degradation over CNAAP30% is proposed in Fig. 7b. Under visible-light irradiation, g-C₃N₄, Ag₃PO₄, and RhB molecules could be excited as the band gap of 2.81 eV, 2.38 eV, and LUMO–HOMO gap of 2.23 eV [49,50], respectively. The LUMO and HOMO of RhB molecules is −5.43 eV and −8.266 eV [49], respectively, its standard electrode potential of LUMO vs. NHE is calculated to be −0.95 eV which is positive than the CB of g-C₃N₄.

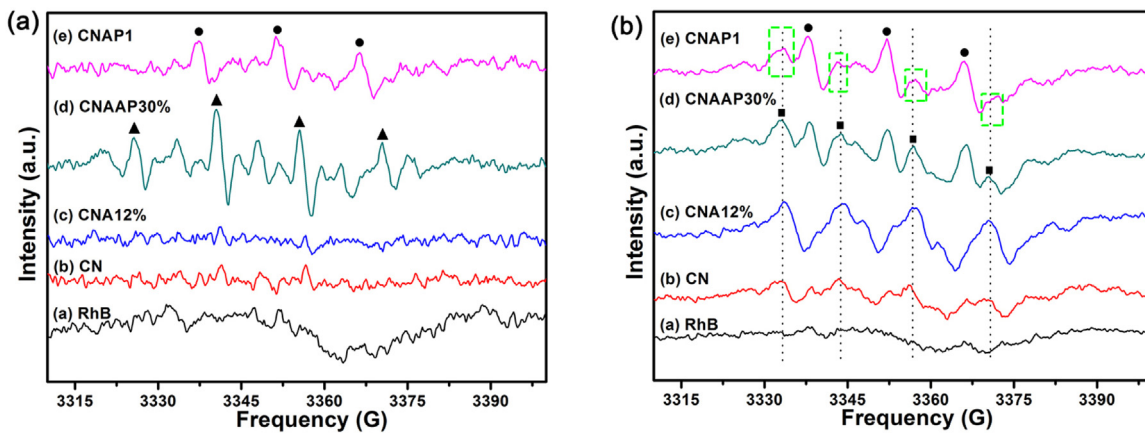


Fig. 6. EPR spectra of DMPO-•OH (a) and DMPO-•O₂⁻/OOH (b) adducts of CN, CNA12%, CNAAP30%, and CNAP1 under visible light irradiation.

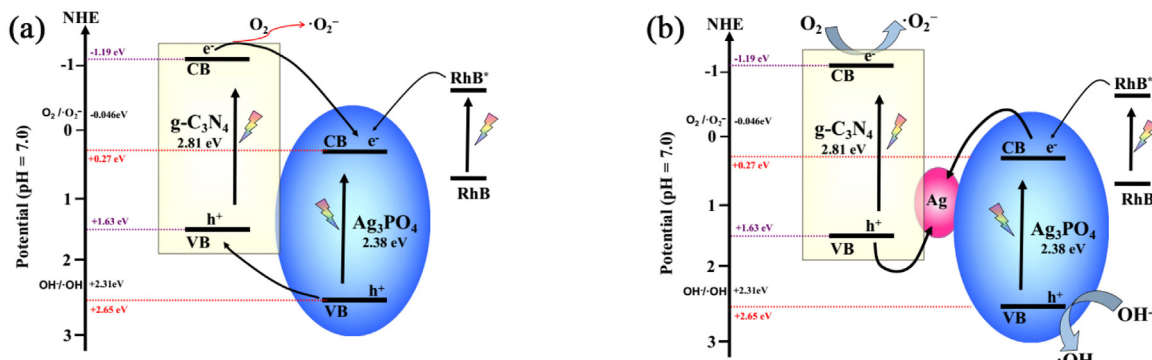


Fig. 7. Schematic illustration for the charge separation and transfer of g-C₃N₄@Ag₃PO₄ (a) and Z-scheme g-C₃N₄@Ag@Ag₃PO₄ (b).

(−1.12 eV vs. NHE), indicating the photoexcited electrons from RhB molecules could not overpass energy barrier to inject into g-C₃N₄, therefore, the photoexcited electrons from RhB molecules could only injected to the CB of Ag₃PO₄ (+0.27 eV vs. NHE) [49,50], as shown in Fig. 7. Compared with CNAP1 hybrids, CNAAP30% have signals of both DMPO-•OH adducts and DMPO-•O₂⁻/OOH adducts, suggesting that g-C₃N₄@Ag@Ag₃PO₄ does not follow the double-transfer mechanism like g-C₃N₄@Ag₃PO₄, as shown in Fig. 7a. Otherwise, it is impossible to generate both hydroxyl radicals and superoxide radicals. The possible photocatalytic mechanism in the g-C₃N₄@Ag@Ag₃PO₄ system is believed to follow a Z-scheme mechanism [37,40,41,51,52], as shown in Fig. 7b. Ag nanoparticles embedded in the interface of g-C₃N₄ and Ag₃PO₄ might act as a charge transmission bridge to efficiently facilitate recombination of the holes on the VB of g-C₃N₄ with the electrons on CB of Ag₃PO₄, as well as enhancing the separation of electron-hole pairs [40,41,53]. Fan et al. recently reported that because the CB edges of Ag₃PO₄ are more negative than the Fermi level of metallic Ag, the photo-generated electrons in the CB of Ag₃PO₄ shift to metallic Ag. Simultaneously, the holes in the VB of g-C₃N₄ move to metallic Ag and combine with the electrons [37]. While, as shown in Fig. 7b, the electrons remaining in the CB of g-C₃N₄ (−1.19 eV vs. NHE) could reduce O₂ to •O₂⁻ since its CB potential is more negative than E₀ (O₂/[•]O₂⁻) (−0.046 eV vs. NHE) [54]. The holes remaining in the VB of Ag₃PO₄ (+2.65 eV vs. NHE) can reduce OH⁻ to •OH [37,55].

3.4. In-situ photocalorimetry-fluorescence spectroscopy studies of photocatalytic performance and degradation pathway

Fig. 8a presents the heat changes curves of RhB photocatalysis over CN, CNAP1, and CNAAP30%. Three main heat changes

of CNAAP30% occurred during the RhB photocatalysis: (ab) the photoresponse of Rhodamine B molecules and photocatalysts, consequently generating both hydroxyl and superoxide radicals, (bc) the balance between endothermic photoresponse and exothermic RhB photodegradation by O₂⁻/•OH as well as (cd) a stable exothermic period of RhB photodegradation after about 20 min of visible light irradiation. The heat changes of each stage is determined by integrating area of its heat change curve of the corresponding stage, as shown in Table 1. Generally, the reaction heat liberated during photocatalysis is directly proportional to the concentration of RhB molecules reacted in the system [7]. As for CNAAP30%, the integrated apparatus underwent an initial endothermic reaction and a subsequent exothermic stage, and finally maintained a stable exothermic cd stage with a pseudo-zero-order process. The heat changes of stages (ab), (bc), (cd), and (ad) are 0.0502, −0.00691, −1.0977, and −1.0544 J, respectively. The sum liberated heat of CNAAP30% in Table 1 is almost 2.85 times higher than that of the CN and 1.39 times higher than that of CNAP1 within visible light irradiation of one hour. Within a same irradiation time, the more heat releases, the higher photocatalytic efficiency is. The slow exothermic stage of RhB under the visible light irradiation in Fig. 8a may be derived from the heat release of photoexcited RhB molecules.

The rate of photocatalysis (R_t) is related directly to the rate of heat changes (dQ_t/dt) by the following [7]:

$$R_t = \frac{d\xi}{dt} = \frac{(dQ_t/dt)}{\Delta Q_0^{\text{theor}}} \quad (1)$$

where ΔQ_t is the reaction heat released at time t and $\Delta Q_0^{\text{theor}}$ is the theoretical heat for complete photodecomposition of RhB over a photocatalyst.

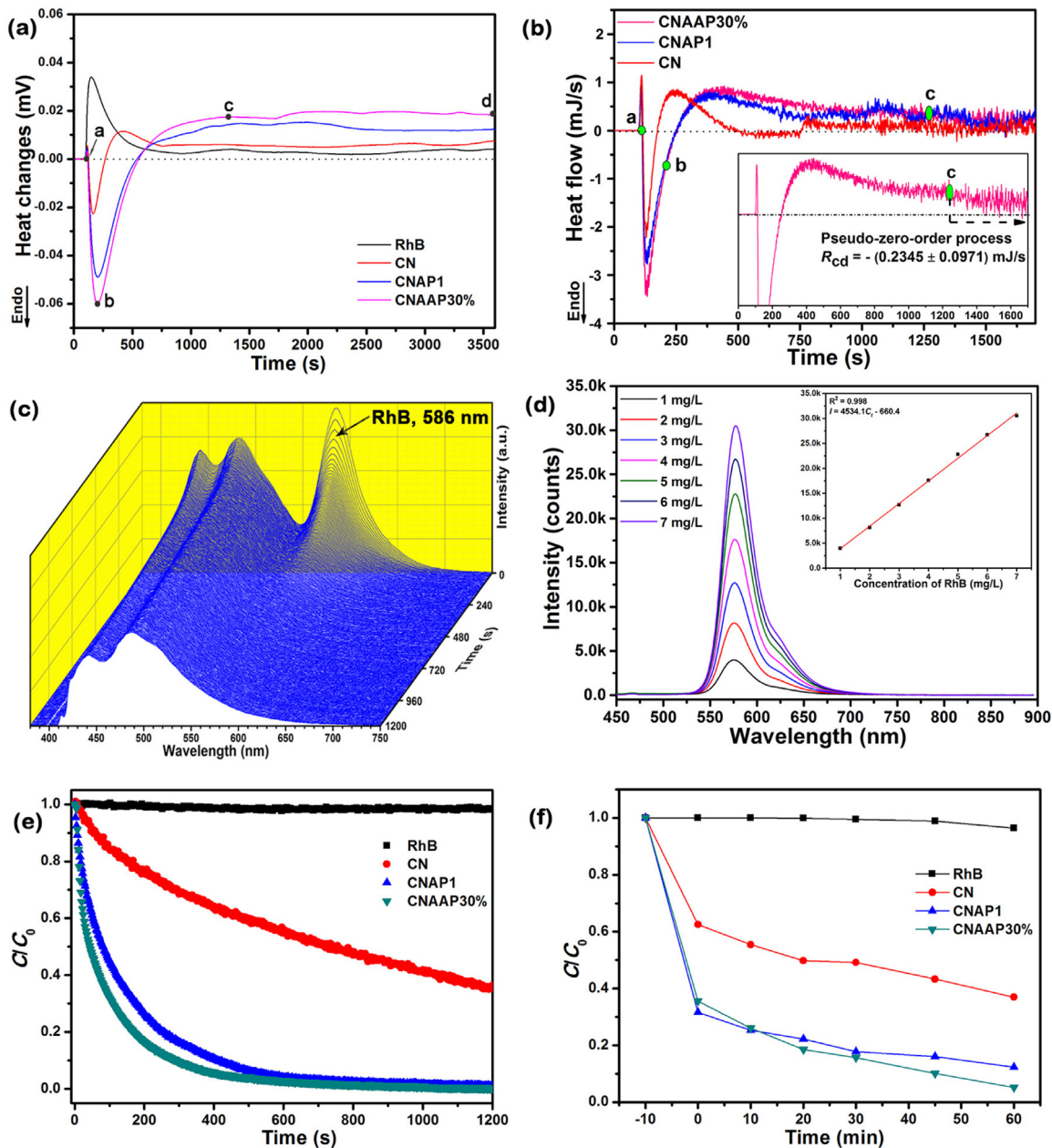


Fig. 8. Heat changes (a) and heat flow curves of RhB photocatalysis over CN, CNAP1, and CNAAP30%, fluorescence intensity vs. wavelength (nm) vs. time (s) image of photocatalytic degradation of RhB over CNAAP30% (c), standard curve of fluorescence intensity of RhB aqueous solution vs. concentration (d), and plots of C/C_0 vs. time detected by *in situ* 3D fluorescence spectra (e) and detected by UV-vis spectrum of RhB photocatalysis over CN, CNAP1, and CNAAP30%.

As for dQ/dt , it could be derived from the heat changes curves (E_t-t) of RhB photocatalysis by following:

$$P_t = \frac{E_t}{S} \quad (2)$$

where P_t is power at time t and E_t is the thermoelectric power at time t in the heat changes curves, S is the calorimetric constant of photocalorimeter which is determined to be $(69.91 \pm 0.56) \mu\text{V mW}^{-1}$ at 298.15 K in the supporting information.

According to Joule's law, the rate of heat changes (dQ_t/dt) could be derived by the following:

$$R = \frac{dQ_t}{dt} = \frac{t \cdot (dE_t/dt)}{S} + E_t/S \quad (3)$$

Fig. 8b shows the heat flow curves of RhB photocatalysis over CN, CNAP1, and CNAAP30%, the corresponding stable exothermic

rate of cd stage is presented in Table 1. As for CNAAP30%, the a stable exothermic rate in cd stage with a pseudo-zero-order process is $-(0.2345 \pm 0.0971) \text{ mJ s}^{-1}$, which is almost 4.55 times higher than that of the CN and 1.04 times higher than that of CNAP1. Gaisford et al. demonstrated that photocalorimetry is generally applicable to zero-order processes in the photodegradation of nifedipine, and reported that the number of molecules of nifedipine reacting per unit time must be the same under a constant light power, irrespective of the volume used [56]. It is important to note that the mixture solution containing 0.25 mg mL^{-1} CNAAP30% is an almost homogeneous aqueous solution without a light path under irradiation of the 405 nm laser (as shown in Fig. S12). Therefore, almost all the photocatalysts NPs are exposed under the incident light, resulting in the number of activated photocatalysts being constant. When irradiated for 1240 s (denoted by c) in Fig. 8a, this results in a certain amount of active species ($\text{O}_2^\bullet/\text{OH}$) being generated per unit of

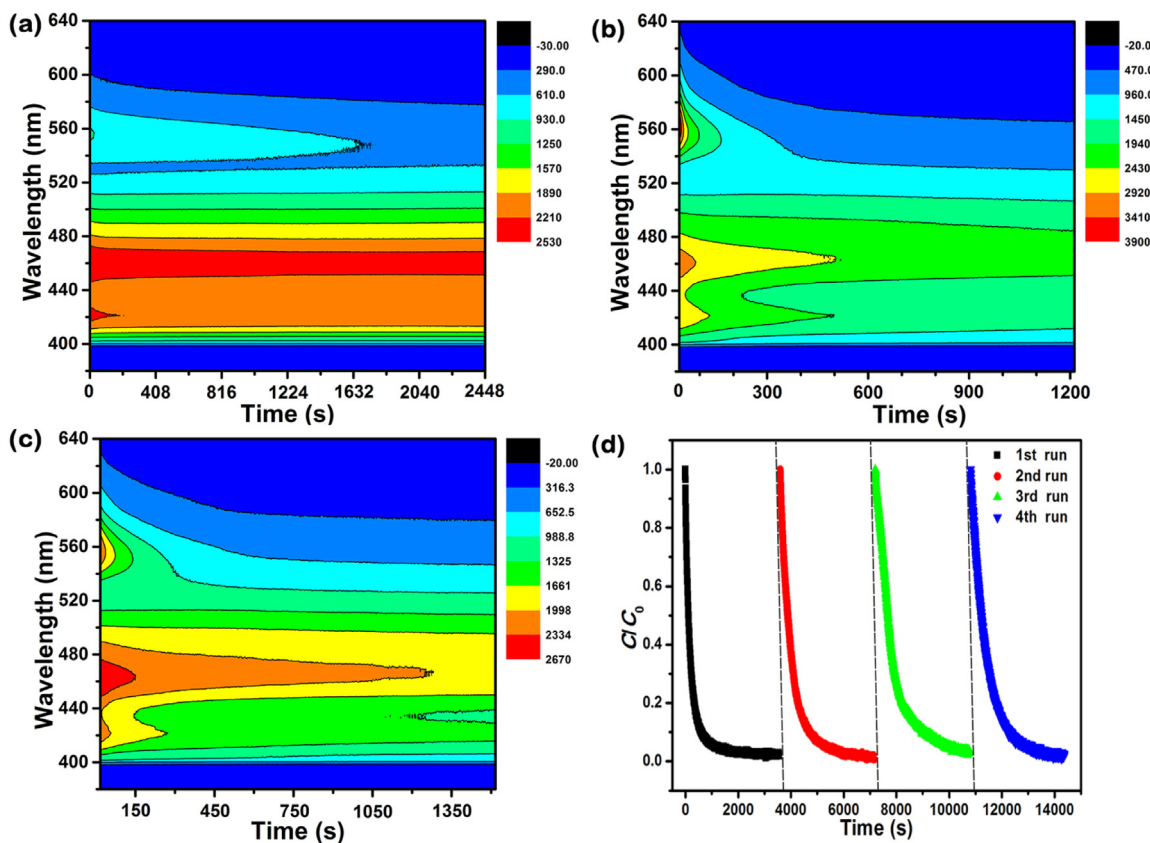


Fig. 9. Contour map of fluorescence intensity vs. wavelength (nm) vs. time (s) of photocatalytic degradation of RhB over CN (a), CNAAP30% (b), and CNAP1 (c) under visible light irradiation, recycle experiment (d) of CNAAP30% under 60 min of 405 nm laser irradiation.

time, which determines directly the exothermic rate and provides a stable organic photooxidation rate per unit of time.

The fluorescence intensity vs. wavelength (nm) vs. time (s) image of photocatalytic degradation of RhB over CNAAP30% is shown in Fig. 8c. The peak at 586 nm is attributed to the chromophore of RhB, being in agreement with the peak in Fig. 8d, while those at 442 and 482 nm were attributed to g-C₃N₄. The standard curve of fluorescence intensity of RhB aqueous solution vs. concentration in Fig. 8d is a good linear relationship in the concentration of RhB ranging from 0 to 7 mg L⁻¹. As for 5 mg L⁻¹ of the initial concentration of RhB in this work, according to the Lambert-Beer law, plots of C/C_0 vs. time were derived from the corresponding fluorescence intensity vs. wavelength (nm) vs. time (s) image. After 10 min, the degradation efficiency of the chromophore of RhB in Fig. 8e increased to 97.5%, which is 2.26 times higher than that of the CN. The degradation efficiency the chromophoric groups detected by UV-vis spectra in Fig. 8f also shows that CNAAP30% exhibited higher photocatalytic efficiency and the degradation efficiency is up to 94.8% after 60 min of irradiation, which was much higher than for both CNAP1 and CN. Meanwhile, compared with both CN and CNAP1, the contour map of fluorescence intensity vs. wavelength (nm) vs. time (s) of the photocatalytic degradation of RhB over CNAAP30% in Fig. 9b dramatically changes from red to blue at 586 nm within 10 min, indicating that the RhB is rapidly degraded. The recycle experiment of CNAAP30% after 60 min of 405 nm laser irradiation in Fig. 9d shows that the degradation efficiency still reaches over 98% after four cycles, indicating that the catalyst is stable.

When irradiated for 20 min, the chromophore of RhB almost completely degrades in Fig. 8e, indicating the heat changes of CNAAP30% in stage cd in Fig. 8a release from the degradation of

intermediates. To further confirm this result, UPLC-ESI-MS/MS was used to detect and identify polar degradation products, such as RhB and N-demethylated intermediates, under different irradiation times. According to UPLC chromatograms in Fig. 10, Peaks A (t_R 5.93 min), B (t_R 4.97 min), C (t_R 6.38 min), D (t_R 3.84 min), E (t_R 2.94 min) and F (t_R 7.15 min) were derived from maternal RhB, N,N-diethyl-N-ethylrhodamine (DER), N-ethyl-N-ethylrhodamine (EER), N,N-diethylrhodamine (DR), N-ethylrhodamine (ER) and rhodamine (R), respectively, which were confirmed by LC/MS/MS identification in Fig. S14 and presented in Table S2. Peak A (t_R 5.93 min) of the RhB dye is rapidly decreased within 10 min, indicating that intermediates containing chromophores are rapidly degraded by CNAAP30% in 10 min, which is in agreement with the results detected by the *in-situ* fluorescence spectrum in Fig. 8e. After irradiation for 10 min, several new absorption peaks (indicated by the red dotted oval in Fig. 9) in ESI mass spectra were detected in 20 and 60 min, indicating that the photocatalytic degradation of RhB over CNAAP30% is still going, and ring opening and mineralization of the intermediates derived from chromophore occur with a rate-determining step after about 20 min.

The zeta potential of CNAAP30% nanoparticles in Fig. S4 ranges from -28.23 to -49.49 mV when the pH changes from 5 to 9, forming a type of colloidal solution with a negatively charged surface in aqueous solution. When mixed with RhB and N-de-ethylated intermediates, which are cationic dyes, the surface adsorption mode of RhB and N-de-ethylated intermediates on the surface of CNAAP30% is formed, as shown in Fig. S15, and eventually facilitating photocatalytic activity and resulting in higher contents of EER and lower contents of ER. Finally, the generated hydroxyl and superoxide radicals decomposes pollutants with two competitive processes in Fig. 11, where N-demethylation and chromophore cleavage [57–60]

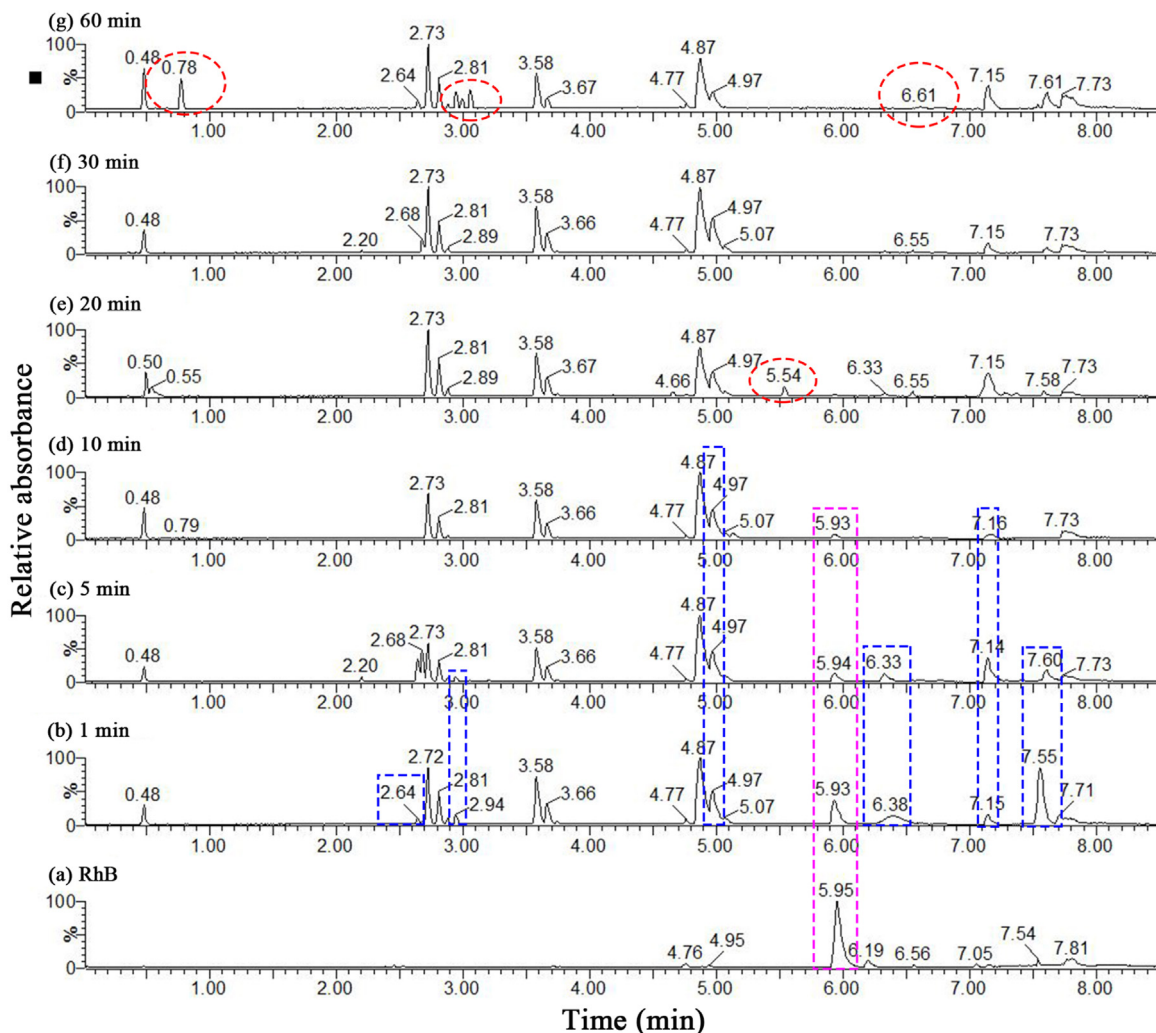


Fig. 10. ESI mass spectra of *N*-de-ethylated intermediates from the degradation of RhB over Z-scheme $\text{g-C}_3\text{N}_4@\text{Ag}@\text{Ag}_3\text{PO}_4$ detected by LC/MS/MS.

occur simultaneously in the presence of $\text{h}^+/\text{O}_2^\bullet-/^\bullet\text{OH}$ in a stepwise manner within 20 min. After this, ring opening and mineralization occur with a rate-determining step, and finally and optimally converted to inorganic products (e.g., CO_2 and water) [56], which is in agreement with the result in cd stage with a pseudo-zero-order process (as shown in Fig. 8a). As for the whole stages, including (ab) the photoresponse of Rhodamine B molecules and the photocatalyst, (bc) the balance between endothermic photoresponse and exothermic RhB photodegradation by $\text{O}_2^\bullet-/^\bullet\text{OH}$ as well as (cd) a stable exothermic period of RhB photodegradation, the reaction order of photocatalysis is determined by the rate-determining step in cd stage rather than by the variation of chromophoric groups vs. time only in the beginning of photocatalysis. Therefore, the ring cleavage and the oxidation of the intermediates in cd stage with a pseudo-zero-order process is the rate-determining step, resulting in a pseudo-zero-order rather than a first-order process in RhB photocatalysis over Z-scheme $\text{g-C}_3\text{N}_4@\text{Ag}@\text{Ag}_3\text{PO}_4$ nanojunctions.

4. Conclusions

This work demonstrates the feasibility of *in situ* photocalorimetry-fluorescence spectroscopy to investigate not only the photocatalytic kinetics but also reaction pathway and the rate-determining step. In this study, we used the photocalorimetry-fluorescence spectrum, coupling of a photocalorimeter and a laser-induced fluorescence spectroscopy, to demonstrate it is a

pseudo-zero-order rather than a first-order process. During RhB photocatalysis over $\text{g-C}_3\text{N}_4@\text{Ag}@\text{Ag}_3\text{PO}_4$, three main heat changes occurred: (ab) the photoresponse of Rhodamine B molecules and the photocatalyst, consequently generating both hydroxyl and superoxide radicals, (bc) the balance between endothermic photoresponse and exothermic RhB photodegradation by $\text{O}_2^\bullet-/^\bullet\text{OH}$ as well as (cd) a stable exothermic period of RhB photodegradation after about 20 min. The heat changes of stages (ab), (bc), (cd), and (ad) were $+0.0502$, -0.00691 , -1.0977 , and -1.0544J , respectively. Specifically, the photocatalysis underwent an initial endothermic reaction and a subsequent exothermic stage, and maintained a stable exothermic rate of $-(0.2345 \pm 0.0971)\text{mJ s}^{-1}$ with a pseudo-zero-order process, which is almost 4.55 times higher than that of the CN and 1.04 times higher than that of CNAP1. As a result of Ag NPs working as a bridge, the $\text{g-C}_3\text{N}_4@\text{Ag}@\text{Ag}_3\text{PO}_4$ system followed a Z-scheme mechanism, simultaneously generating both hydroxyl and superoxide radicals. Therefore, *N*-demethylation and chromophore cleavage rapidly occur within 10 min under visible-light irradiation. After that, the ring cleavage and the oxidation of intermediates which were the rate-determining step dominated, corresponding to the cd stage with a pseudo-zero-order process, and resulting in a pseudo-zero-order rather than a first-order process in RhB photocatalysis over $\text{g-C}_3\text{N}_4@\text{Ag}@\text{Ag}_3\text{PO}_4$. Thus, this novel integrated technology can effectively promote the development of microcalorimetry in spectroscopy and optical thermochemistry. In addition, this system can be widely applied

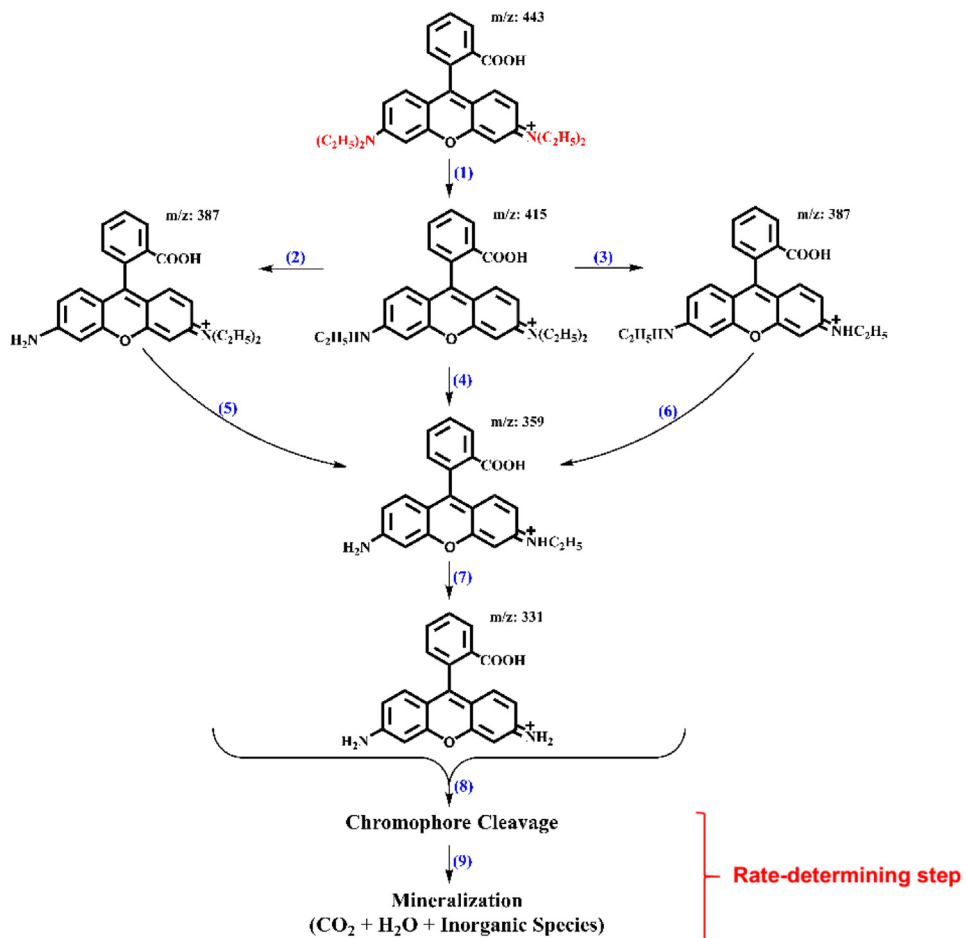


Fig. 11. Degradation pathway of RhB dye over Z-scheme $\text{g-C}_3\text{N}_4@\text{Ag}@\text{Ag}_3\text{PO}_4$ nanocomposites.

to many disciplines with multiple functions and high efficiency in chemistry, physics, biology, bionics, medicine and materials science.

Acknowledgements

The authors are thankful for the financial support from the National Natural Science Foundation of China (21273050, 21573048), the Reform of Postgraduate Cultivation Mechanism from 2013 (Chemical Engineering, 113000100030001), Innovation Projects of Postgraduate Education of Guangxi University for Nationalities (gxunchxs2015086), and National Training Programs of Innovation and Entrepreneurship for Undergraduates (20150608040). The authors would like to express their great appreciation to Guangxi Colleges and Universities Key Laboratory of Food Safety and Pharmaceutical Analytical Chemistry (Guangxi University for Nationalities).

Appendix A. Supplementary data

Supplementary data associated with this article can be found at supporting information.

Appendix A. Supplementary data

Supplementary data associated with this article can be found, in the online version, at [10.1016/j.apcatb.2017.05.086](https://doi.org/10.1016/j.apcatb.2017.05.086).

References

- [1] W. Tu, Y. Zhou, Z. Zou, *Adv. Funct. Mater.* 23 (2013) 4996–5008.
- [2] H.L. Wang, L.S. Zhang, Z.G. Chen, J.Q. Hu, S.J. Li, Z.H. Wang, J.S. Liu, X.C. Wang, *Chem. Soc. Rev.* 43 (2014) 5234–5244.
- [3] Q. Liang, Z. Li, X. Yu, Z.H. Huang, F. Kang, Q.H. Yang, *Adv. Mater.* 27 (2015) 4634–4639.
- [4] Y. Qu, X. Duan, *Chem. Soc. Rev.* 42 (2013) 2568–2580.
- [5] Q. Xiang, J. Yu, M. Jaroniec, *Chem. Soc. Rev.* 41 (2012) 782–796.
- [6] H. Li, W. Tu, Y. Zhou, Z. Zou, *Adv. Sci.* (2016) 1500389, <http://dx.doi.org/10.1002/advs.201500389>.
- [7] X. Li, Z. Huang, Z. Liu, K. Diao, G. Fan, Z. Huang, X. Tan, *Appl. Catal. B: Environ.* 181 (2016) 79–87.
- [8] F. Fan, Z. Feng, C. Li, *Acc. Chem. Res.* 43 (2009) 378–387.
- [9] D. Gong, V.P. Subramaniam, J.G. Highfield, *ACS Catal.* 1 (2011) 864–871.
- [10] B. Silvia, G. Elena, A. Giovanni, *Chem. Rev.* 44 (2013) 1736–1850.
- [11] M.J. Derry, L.A. Fielding, N.J. Warren, C.J. Mable, A.J. Smith, O.O. Mykhaylyk, S.P. Armes, *Chem. Sci.* 7 (2016) 5078–5090.
- [12] M. Dhuna, A.E. Beezer, A.C. Morri, *Rev. Sci. Instrum.* 78 (2007) 025105.
- [13] M. Dhuna, A.E. Beezer, J.A. Connor, D. Clapham, C. Courtice, J. Frost, S. Gaisford, *J. Pharmaceut. Biomed.* 48 (2008) 1316–1320.
- [14] J.L. Magee, T.W. Dewitt, F. Smith, *J. Am. Chem. Soc.* 1 (1939) 3529–3533.
- [15] A.W. Adamson, A.V. Hican, *J. Am. Chem. Soc.* 100 (1978) 1298–1300.
- [16] J. Olmsted III, *Rev. Sci. Instrum.* 50 (1979) 1256–1259.
- [17] J. Olmsted III, *J. Am. Chem. Soc.* 102 (1980) 66–71.
- [18] M. Nakashima, A.W. Adamson, *J. Phys. Chem.* 86 (1982) 2910–2912.
- [19] Y. Harel, A.W. Adamson, *J. Phys. Chem.* 91 (1987) 901–904.
- [20] B. Schaarschmidt, I. Lamprecht, *Specialia* 4 (1973) 505.
- [21] A. Cooper, C.A. Converse, *Biochemistry* 15 (1976) 2970–2978.
- [22] A. Cooper, *Nature* 282 (1979) 531–533.
- [23] R.R. Birge, T.M. Cooper, A.F. Lawrence, M.B. Masthay, C. Vasilakis, C.F. Zhang, R. Zidovetzki, *J. Am. Chem. Soc.* 111 (1989) 4063–4074.
- [24] C.E. Corcione, R. Striani, M. Frigione, *Prog. Org. Coat.* 77 (2014) 1117–1125.
- [25] Y. Li, S. Sun, *J. Am. Oil. Chem. Soc.* 91 (2014) 1425–1432.
- [26] K.S. Anseth, R.A. Scott, N.A. Peppas, *Macromolecules* 29 (1996) 8308–8312.
- [27] S.H. Dickens, J.W. Stansbury, K.M. Choi, C.J.E. Floyd, *Macromolecules* 36 (2003) 6043–6053.

- [28] J. Wei, F. Liu, *Macromolecules* 42 (2009) 5486–5491.
- [29] C.A.G. Fernandez, P. Davies, S. Gomez-Barreiro, J.L. Beceiro, *J. Therm. Anal. Calorim.* 102 (2010) 1057–1062.
- [30] E.M. Carstea, J. Bridgeman, A. Baker, D.M. Reynolds, *Water Res.* 95 (2016) 205–219.
- [31] W.M. Ching, D. Rowland, Z. Zhang, A.L. Bourgeois, D. Kelly, G.A. Dasch, et al., *Clin. Diagn. Lab. Immun.* 8 (2001) 409–414.
- [32] L. Yang, G.A. Colditz, *JAMA Internal Medicine* 175 (2015) 1412.
- [33] D. Reynolds, R.I. Nicolson, H. Hamblly, *Dyslexia* 9 (2003) 48–71.
- [34] A.L. Toth, K. Varala, T.C. Newman, et al., *Science* 318 (2007) 441.
- [35] D. Curwen, R. Knight, T.M. Work, et al., *Am. J. Potato Res.* 1 (2011) 1–24.
- [36] X. Ma, P.A. Buffler, R.B. Gunier, et al., *Environ. Health Pers.* 110 (2002) 955–960.
- [37] Y. He, L. Zhang, B. Teng, M. Fan, *Environ. Sci. Technol.* 49 (2015) 649–656.
- [38] Y. Liu, L. Fang, H. Lu, Y. Li, C. Hu, H. Yu, *Appl. Catal. B: Environ.* 115 (2012) 245–252.
- [39] F. Dong, L. Wu, Y. Sun, M. Fu, Z. Wu, S.C. Lee, *J. Mater. Chem.* 21 (2011) 15171–15174.
- [40] S. Zhang, J. Li, X. Wang, Y. Huang, M. Zeng, J. Xu, *ACS Appl Mater. Inter.* 6 (2014) 22116–22125.
- [41] H. Katsumata, T. Sakai, T. Suzuki, S. Kaneko, *Ind. Eng. Chem. Res.* 53 (2014) 8018–8025.
- [42] C. Carmalt, C.J. O'Neill, S.A. Parkin, I.P. Apostilco, K.C. Molloy, *J. Mater Chem.* (2001) 2408–2409.
- [43] F. Dong, L. Wu, Y. Sun, M. Fu, Z. Wu, S.C. Lee, *J. Mater. Chem.* 21 (2011) 15171–15174.
- [44] X. Yang, Z. Chen, J. Xu, H. Tang, K. Chen, Y. Jiang, *ACS Appl Mater. Inter.* 7 (2015) 15285–15293.
- [45] C. Ye, J.X. Li, Z.J. Li, X.B. Li, X.B. Fan, L.P. Zhang, L.Z. Wu, *ACS Catal.* 5 (2015) 6973–6979.
- [46] L. Liu, Y.H. Qi, J.R. Lu, S.L. Lin, W.J. An, Y.H. Liang, W.Q. Cui, *Appl. Catal. B: Environ.* 183 (2016) 133–141.
- [47] L. Liu, L. Ding, Y. Liu, W. An, S. Lin, Y. Liang, W. Cui, *Appl. Catal. B: Environ.* 201 (2017) 92–104.
- [48] D. Jiang, J. Zhu, M. Chen, J. Xie, *J. Colloid. Interf. Sci.* 417 (2014) 115–120.
- [49] T. Yan, J. Tian, W. Guan, Z. Qiao, W. Li, J. You, B. Huang, *Appl. Catal. B: Environ.* 202 (2017) 84–94.
- [50] X. Chang, M.A. Gondal, A.A. Al-Saadi, M.A. Ali, H. Shen, Q. Zhou, et al., *J. Colloid Interf. Sci.* 377 (2012) 291–298.
- [51] S. Shi, M.A. Gondal, A.A. Al-Saadi, R. Fajgar, J. Kupcik, X. Chang, et al., *J. Colloid Interf. Sci.* 416 (2014) 212.
- [52] S. Meng, X. Ning, T. Zhang, S.F. Chen, X. Fu, *Phys. Chem. Chem. Phys.* 17 (2015) 11577–11585.
- [53] S. Bai, J. Jiang, Q. Zhang, Y. Xiong, *Chem. Soc. Rev.* 44 (2015) 2893–2939.
- [54] M. Xiong, L. Chen, Q. Yuan, J. He, S.L. Luo, C.T. Au, S.F. Yin, *Carbon* 86 (2015) 217–224.
- [55] X. Yang, H. Cui, Y. Li, J. Qin, R. Zhang, H. Tang, *ACS Catal.* 3 (2013) 363–369.
- [56] L.A. Sousa, A.E. Beezer, L.D. Hansen, D. Clapham, J.A. Connor, S. Gaisford, *J. Phys. Chem. B* 116 (2012) 6356.
- [57] H.E. Zhong, Y. Shaogui, J.U. Yongming, S.U.N. Cheng, *J. Environ. Sci.* 21 (2009) 268–272.
- [58] S. Hisaindee, M.A. Meetani, M.A. Rauf, *Trac-Trend Anal. Chem.* 49 (2013) 31–44.
- [59] H. Fu, S. Zhang, T. Xu, Y. Zhu, J. Chen, *Environ. Sci. Technol.* 42 (2008) 2085–2091.
- [60] Z. He, C. Sun, S. Yang, Y. Ding, H. He, Z. Wang, *J. Hazard Mater.* 162 (2009) 1477–1486.